Small Methods

small methods
www.small-methods.com

RESEARCH ARTICLE

Machine Learning-Assisted SERS Quantification of Sialylated Alpha-Fetoprotein: From Single-Cell Analysis to Hepatocellular Carcinoma Risk Assessment

Yu Xiao[1,2] | Baolin Li[1] | Chengyao Geng[2] | Yuru Wang[2] | Xiaoqian Wu[2] | Shan Wu[2] | Ye Zhao[2] | Dayu Chen[3] | Feng Yan[3] | Jinbo Liu[1] | Yunlong Chen[2] | Huangxian Ju[1,2]

[1]Department of Medical Laboratory, Affiliated Hospital of Southwest Medical University, Luzhou, China | [2]State Key Laboratory of Analytical Chemistry For Life Science, School of Chemistry, Nanjing University, Nanjing, China | [3]Department of Clinical Laboratory, Nanjing Medical University Affiliated & Cancer Hospital & Jiangsu Cancer Hospital, Jiangsu Institute of Cancer Research, Nanjing, China

Correspondence: Jinbo Liu (liujb7203@swmu.edu.cn) | Yunlong Chen (ylc@nju.edu.cn) | Huangxian Ju (hxju@nju.edu.cn)

Received: 22 March 2026 | **Revised:** 8 June 2026 | **Accepted:** 15 June 2026

Keywords: clinical risk assessment | hepatocellular carcinoma | machine learning | SERS | sialylated alpha-fetoprotein

ABSTRACT

Sialylated alpha-fetoprotein (sAFP) is a very potential marker for the pathogenesis exploration and clinical assessment of hepatocellular carcinoma (HCC). The specific and sensitive quantification of sAFP across multiple aspects is a primary premise. This work constructs a functionalized gold/silver nanocube-encapsulated microgel (Au/AgNC-MG), which can specifically capture sAFP through dual aptamer-based recognition and generate sensitive Raman fingerprints through the heterogeneous bimetallic SERS system. To further improve the specificity and quantifiability of sAFP detection in different scenarios, a series of machine learning (ML) algorithms, including a sAFP classification algorithm, a sAFP image-processing algorithm, and a sAFP-based clinical HCC risk assessment algorithm, were established for sAFP quantification, imaging of single-cell secreted sAFP, and clinical HCC risk assessment from general check-up to cirrhosis clinic patient populations. An online HCC Risk Assessment website is built for the convenience of practical clinical application. The constructed Au/AgNC-MG and established ML algorithms compose a general paradigm for HCC-related laboratory research and clinical applications.

1 | Introduction

Hepatocellular carcinoma (HCC) is a major global health burden, which represents nearly 90% of all primary liver cancer cases [1]. Serum alpha-fetoprotein (AFP) has been broadly applied as a biomarker for HCC risk assessment, but the diagnostic accuracy significantly drops in the early stage of HCC with the serum AFP concentration below 500 ng/mL [2]. Nevertheless, the pathogenesis of HCC exhibits a close association with the glycosylation patterns of AFP, including fucosylation and sialylation [3], which provides an alternative way for accurate assessment of HCC. The fucosylated AFP isoform has been reported to enhance the diagnostic accuracy for some HCC patients [4], while the sialylated AFP (sAFP) is more complex, with marked microheterogeneity including mono-sialylated, di-sialylated species [5], whose diagnostic potential has yet to be explored. Thus, specific and sensitive quantification of sAFP, preferably across multiple aspects from single-cell secretion to patient population samples, can significantly promote the identification of aberrant and hypersecreting tumor cells, and can facilitate accurate

Yu Xiao, Baolin Li and Chengyao Geng contributed equally to this work.

assessment and subsequently personalize the therapeutic program of HCC.

Various methods have been developed for the quantification of sialic acid (Sia) or AFP in serum samples or on cells, including electrochemical sensing [6], fluorescence assays [7], and mass spectrometry analysis [8]. Some of the methods have offered excellent quantification sensitivity, but the specificity is still determined by the recognition ligands, such as lectins [9], antibodies [10], molecularly imprinted polymers [11], and aptamers [12, 13]. As the quantification of sAFP from single-cell secretion to patient population samples poses higher demands for dual specificity and ultrahigh sensitivity with extra single-cell imaging capability, surface-enhanced Raman scattering (SERS) offers the best solution for sAFP quantification owing to its high sensitivity [14, 15], label-free fingerprint specificity [16] and exceptional spatial resolution in Raman imaging [17]. The SERS-based droplet microfluidic platforms have enabled sensitive and high-throughput detection of cancer-related biomarkers, highlighting the potential of integrating SERS with microfluidic compartments for biosensing applications [18, 19]. However, these methods still face notable sensitivity and specificity challenges in complex biological environments due to the inherently non-selective amplification of all molecules within plasmonic hotspots and the complex and overlapping Raman fingerprint spectra. The introduction of new SERS substrates and fingerprint spectral processing approaches is a key solution.

The gold/silver nanocubes (Au/AgNCs) are newly developed SERS substrates [20, 21], which display highly stable and predictable localized surface plasmon resonance performance and uniform crystal facets compared with traditional gold/silver nanoparticles [22]. Notably, AgNCs offer stronger electromagnetic enhancement in the visible spectral range, whereas AuNCs provide superior chemical stability and biocompatibility [23, 24]. Compared with the core-shell structured bimetallic nanocubes [25], the clamping of the target molecule by AgNC and AuNC can coincide with the strongest bimetallic electromagnetic hotspots and exploit chemical enhancement more efficiently [21]. Combined with the rapidly developing machine learning (ML) assisted spectral analysis, this work constructed a functionalized Au/AgNCs microgel (Au/AgNC-MG) and established a series of ML algorithms to process the data of different SERS detection modes, which achieve specific and sensitive quantification of sAFP across multiple aspects from the single-cell secretion to patient population samples.

To equalize the electromagnetic enhancements of the protein and glycan portions in sAFP, the Au/AgNCs were respectively modified with AFP- and Sia- specific aptamers (Apt1 and Apt2, Table S1) through polyA to obtain AuNC-Apt1 and AgNC-Apt2 [12, 13], which were simultaneously encapsulated into a hydrogel microsphere through a microfluidic chip by using the polyethylene glycol diacrylate (PEGDA) aqueous and hexadecane (Oil) (Scheme 1A) [26]. After ultraviolet irradiation, the network pores of the obtained Au/AgNC-MG can maintain the diffusion of the internal Au/AgNCs and size-selectively transmit sAFP, which can specifically connect the AuNC and AgNC to form a heterogeneous bimetallic Au-AgNC nanostructure with ultrastrong SERS plasmonic hotspots, and resist the influence of other larger biomolecules in biological environments (Scheme 1A). To further improve the specificity of sAFP detection, a sAFP classification algorithm (sAFP-CLA) was established based on the support vector machine (SVM) model and trained by incubating the Au/AgNC-MG with standard sAFP samples. The Raman signals of the clinical serum samples detected by Au/AgNC-MG were classified by sAFP-CLA with prespecified performance criteria before quantification. To quantify the single-cell secreted sAFP, the singly seeded cell was incubated with Au/AgNC-MG densely (Scheme 1B). The secreted sAFP can be specifically captured by the Au/AgNC-MG surrounding the cell and generate a SERS signal. A sAFP image-processing algorithm (sAFP-IPA) was further established based on sAFP-CLA and global Otsu thresholding analysis, which can generate the concentration map of the single-cell secreted sAFP. In addition, a sAFP based clinical HCC risk assessment algorithm (sAFP-RAA) was also established based on logistic regression model and trained by the Raman spectra collected from serum samples of different patient populations and healthy individuals after Au/AgNC-MG incubation (Scheme 1C), which achieves excellent decision curve analysis (DCA) performances for general check-up and cirrhosis clinic patient populations reported by the American Association for the Study of Liver Diseases (AASLD). Furthermore, an online HCC Risk Assessment website was built with the sAFP-RAA containing a backend and an easy user interface for convenient and practical clinical use. The constructed Au/AgNC-MG and established ML algorithms compose a general paradigm for the quantification of sAFP from single-cell secretion to patient populations, which provides a comprehensive platform covering multiple aspects from laboratory research to clinical applications.

2 | Results and Discussion

2.1 | Construction and Characterization of Au/AgNC-MG

AuNCs and AgNCs were prepared according to previous reports [27, 28] and characterized by TEM images (Figure S1), which revealed uniform cubic structures with side lengths around 90 nm. The Apt1 and Apt2 were respectively modified onto AuNCs and AgNCs through the interaction between polyadenines (poly A) and the metal surface [29], which was characterized by UV–vis absorption spectra (Figure S2) and zeta potential analysis (Figure S3). To maintain the stability and reduce the nonspecific adsorption of the nanocube probes, the Au/AgNCs were first modified with mercaptopoly (ethylene glycol) carboxylic acid (HS-PEG-COOH). Uniform and blue-shifted absorbance peaks were observed in both AuNC-PEG and AgNC-PEG solutions (Figure S2), indicating the damped high-energy band and improved colloidal dispersion after the PEG modification [30]. After further modification with poly A-containing aptamers, although the characteristic nucleic acid peak at 260 nm was not prominent, the extra blue shifts of the absorbance peak also demonstrated the successful modification of aptamers on AuNC-Apt1 and AgNC-Apt2 [31]. In addition, the zeta potential shifted from positive to negative (Figure S3), which further demonstrated the successful modification of Apt1 and Apt2 onto AuNCs and AgNCs.

The SERS-enhancing capability of the designed bimetallic system was investigated by Raman detection of the standard sAFP sample

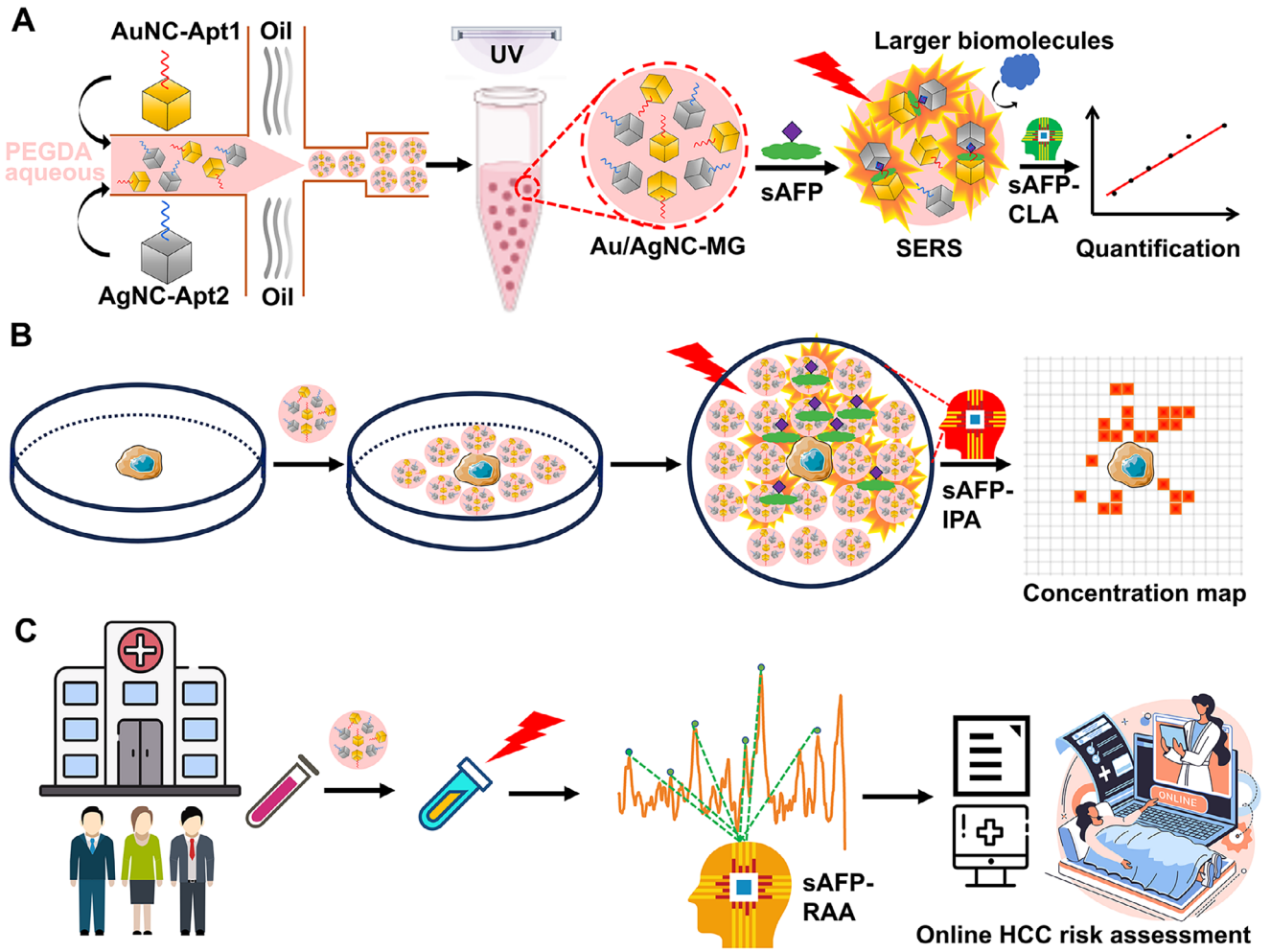

SCHEME 1 | Schematic illustration. (A) Preparation of Au/AgNC-MG. AuNC-Apt1 and AgNC-Apt2 were simultaneously encapsulated into a hydrogel microsphere through a microfluidic chip using PEGDA aqueous and Oil. The Au/AgNC-MG was obtained after ultraviolet irradiation and used for quantification of sAFP assisted by sAFP-CLA. (B) In situ quantification of single-cell secreted sAFP. The singly seeded cell was densely incubated with Au/AgNC-MG. The secreted sAFP was captured by Au/AgNC-MG around the cell to generate a SERS signal, which was processed by sAFP-IPA to generate the sAFP concentration map. (C) Clinical HCC risk assessment. The sAFP-RAA was established and trained by the Raman spectra collected from serum samples of different patient populations and healthy individuals after Au/AgNC-MG incubation, which was further used to build the online HCC risk assessment website.

incubated with different combinations of the Apt1/2 modified Au/AgNC probes under 785 nm excitation (Figure S4). The standard sAFP sample is commercially available and produced via recombinant DNA technology using human embryonic kidney cells [32]. The coding region of sAFP (amino acids 1–605) contains one glycosylation site, which often exhibits heterogeneous glycosylation profiles [33]. The Sia within the standard sAFP sample was first characterized by chemical colorimetric analysis using sodium periodate ($NaIO_4$) oxidation (Figure S5) [34]. After treatment with $NaIO_4$ and then Schiff reagent, the supernatant of PNGase F-treated standard sAFP, Sia, and standard sAFP exhibited a deep purple color with strong UV absorption peaks around 520 nm, while the precipitate of PNGase F-treated standard sAFP exhibited light purple color and negligible UV absorption peaks, indicating the presence of Sia in the standard sAFP. According to the finite-difference time-domain (FDTD) simulation (Figure S6), a 5-nm interparticle gap with the Au/AgNC heterogeneous bimetallic structure could achieve a normalized electric-field amplitude to 31.3, indicating a highly efficient SERS enhancement to sAFP. When performing the actual sample testing, the standard sAFP incubated with AuNC-Apt1/2 and AgNC-Apt1/2 exhibited a 10 times higher Raman intensity compared to those incubated with the monometallic systems of AgNC-Apt1/2 and AuNC-Apt1/2 (Figure S4), which further indicated the excellent SERS performance of the designed bimetallic system.

The Au/AgNC-MG was prepared by injecting an aqueous phase containing AuNC-Apt1, AgNC-Apt2, PEGDA, and photoinitiator into a microfluidic chip with an oil-to-water flow rate ratio of 3:1 (Figure S7A). The droplets with a diameter of around 30 μm were generated with a clear oil shell, which could be observed under an optical microscope (Figure S7B). After ultraviolet irradiation and ethanol washing, the oil layer disappeared (Figure S7C), and the obtained Au/AgNC-MG exhibited an obvious reticular structure in the SEM image (Figure S7D). The size distribution of Au/AgNC-MG was analyzed by optical microscopy and quantified by ImageJ (Figure S8), which exhibited a relatively concentrated diameter distribution between 25 to 30 μm with

an average diameter of 30.2 ± 9.9 μm. Besides, the SEM-based energy-dispersive x-ray spectroscopy (EDS) elemental mapping of individual Au/AgNC-MG indicated a uniform distribution of Au and Ag elements (Figure S9), which demonstrated the successful encapsulation and uniform distribution of Au/AgNC probes for the reliable Raman detection. The size-selective exclusion of large biomolecules by Au/AgNC-MG was investigated by incubating Au/AgNC-MG with different molecular weight fluorescein isothiocyanate-dextran (FITC-dextran). After incubation for 4 h and then subjected to confocal laser scanning microscopy (CLSM) imaging (Figure S10), obvious FITC fluorescence was observed within the Au/AgNC-MG incubated with 10 and 70 kDa FITC-dextran, while those incubated with 150 kDa FITC-dextran only exhibited weak FITC fluorescence at the periphery of the microgels, demonstrating the capability of size-selective exclusion of large biomolecules by Au/AgNC-MG. The background Raman signals of Au/AgNC-MG were investigated by direct Raman detection under 785 nm excitation, which exhibited a weak PEGDA characteristic peak at 890 cm^{-1} attributed to C—O—C/C—C vibrations of the polymer backbone. The background Raman spectra of Au/AgNC-MG remained unchanged after storing at 4°C for 1–3 weeks (Figure S11), demonstrating its excellent stability.

The sAFP detecting capability of Au/AgNC-MG was investigated by incubating the standard sAFP, PNGase F-treated standard sAFP, and Sia with Au/AgNC-MG at 37°C for 2 h and subjected to Raman detection, respectively (Figure S12). After a careful comparison of the three spectra, the PNGase F-treated standard sAFP exhibited distinct Raman peaks at 500, 650, 1100, and 1185 cm^{-1}, which could be attributed to its disulfide bonds predominantly in the g-g-g conformation. Sia exhibited distinct Raman peaks at 890 and 1035 cm^{-1}, which could be attributed to glycosidic C—O—C and C—OH stretching vibrations. Other overlapping peaks around 720 and 1435 cm^{-1} may arise from free Sia and glycosidically bound Sia or background features, which were typically negligible and did not interfere with peak assignment. Detailed vibrational assignments are shown in Table S2 [35–39]. These characteristic peaks all appeared in the spectrum of standard sAFP, which demonstrated the sAFP detecting capability of Au/AgNC-MG and the potential to classify sAFP by Raman fingerprint.

2.2 | Classification of sAFP

To achieve the classification of sAFP from other glycoproteins in complex biological environments, the sAFP-CLA was established and trained with standard sAFP and a mixed other glycoprotein (oGP) sample (Figure 1A). The oGP was composed of carcinoembryonic antigen (CEA), bovine serum albumin (BSA), and AFP-depleted cell culture supernatants. CEA served as a structural analog, sharing similar molecular size and exhibiting an even higher degree of glycosylation than sAFP [40]. BSA was selected to simulate the abundant albumin background typical of human serum, whereas sAFP-depleted supernatants served as a reference for distinguishing sAFP from other secreted proteins in the cell culture environment. After incubating each compound with Au/AgNC-MG at 37°C for 2 h, followed by Raman detection, significantly different Raman fingerprints were observed, with the most remarkable peak differences at 500 and 1035 cm^{-1} (Figure S13), indicating the representativeness of the training samples.

To train sAFP-CLA, the raw Raman spectral data collected from the Au/AgNC-MG incubated sAFP and oGP were firstly fitted using Whittaker smoothing (Figures 1A-1) [41], which were subsequently processed for feature extraction (Figures 1A-2) and model training using multiple machine learning models (Figure 1A-3) including SVM, random forest (RF), XGBoost, and LightGBM. According to the standard classification reports including *precision*, *recall*, and *F1-score* (Figure 1B), the SVM model-based sAFP-CLA achieved the highest classification accuracy of 91%, outperforming the other models in overall predictive performance. To classify sAFP, the unknown spectra collected from different samples after incubation with Au/AgNC-MG were subjected to the trained sAFP-CLA for classification (Figure 1A-4). The confusion matrix exhibited an overall classification accuracy of over 90% (Figure 1C), and the SVM decision boundary (dashed line) in the t-distributed stochastic neighbor embedding (t-SNE) map accurately delineated the classes of sAFP (blue) and oGP (red) (Figure 1D). In addition, the cross-validation accuracy in the learning curve improved from ∼70% to ∼90% with an increasing training dataset size (Figure 1E), which indicated the enhanced model generalization capability and the effective feature discrimination and classification by the SVM-based sAFP-CLA.

The contribution of spectral features identified by sAFP-CLA was obtained by feature analysis (Figure 1F). The positive feature contribution indicated a stronger association with sAFP, whereas the negative feature contribution was associated with oGP. The peak at 500 cm^{-1} exhibited the highest positive feature contribution, which was chosen as the sAFP characteristic peak for quantification analysis. After incubating different concentrations of standard sAFP with Au/AgNC-MG at 37°C for 2 h, followed by Raman detection, the Raman intensity at 500 cm^{-1} exhibited a good linear relationship with sAFP concentrations (Figure S14), indicating the sAFP quantification capability of Au/AgNC-MG. The intra-assay and inter-assay tests respectively, exhibited RSD values of 9.46% and 14.62%, demonstrating the acceptable reproducibility for sAFP quantification (Figure S15). Besides, compared with direct incubation with the mixture of AuNC-Apt1 and AgNC-Apt2, the incubation with Au/AgNC-MG exhibited better selectivity for sAFP (Figure S16), demonstrating the enhanced selectivity by the gel encapsulation.

2.3 | In Situ Quantification of Single-Cell Secreted sAFP

Since the established sAFP-CLA could be successfully used for the classification and quantification of sAFP, it was further used to quantify, in situ, single-cell-secreted sAFP from the human HCC cell line HepG2 (Scheme 1B). The clinical HCC drug sorafenib [42] treated HepG2 and the sAFP-free murine melanoma B16 cells were chosen as controls. Sorafenib can suppress the expression of AFP through the inhibition of multiple kinases [42]. After singly-seeded cells were incubated with 1.8×10^7 particles/mL of Au/AgNC-MG at 37°C, they were directly subjected to confocal laser scanning Raman (CLSR) imaging after incubation for 14, 16, and 18 h (Figure S17A). Based on

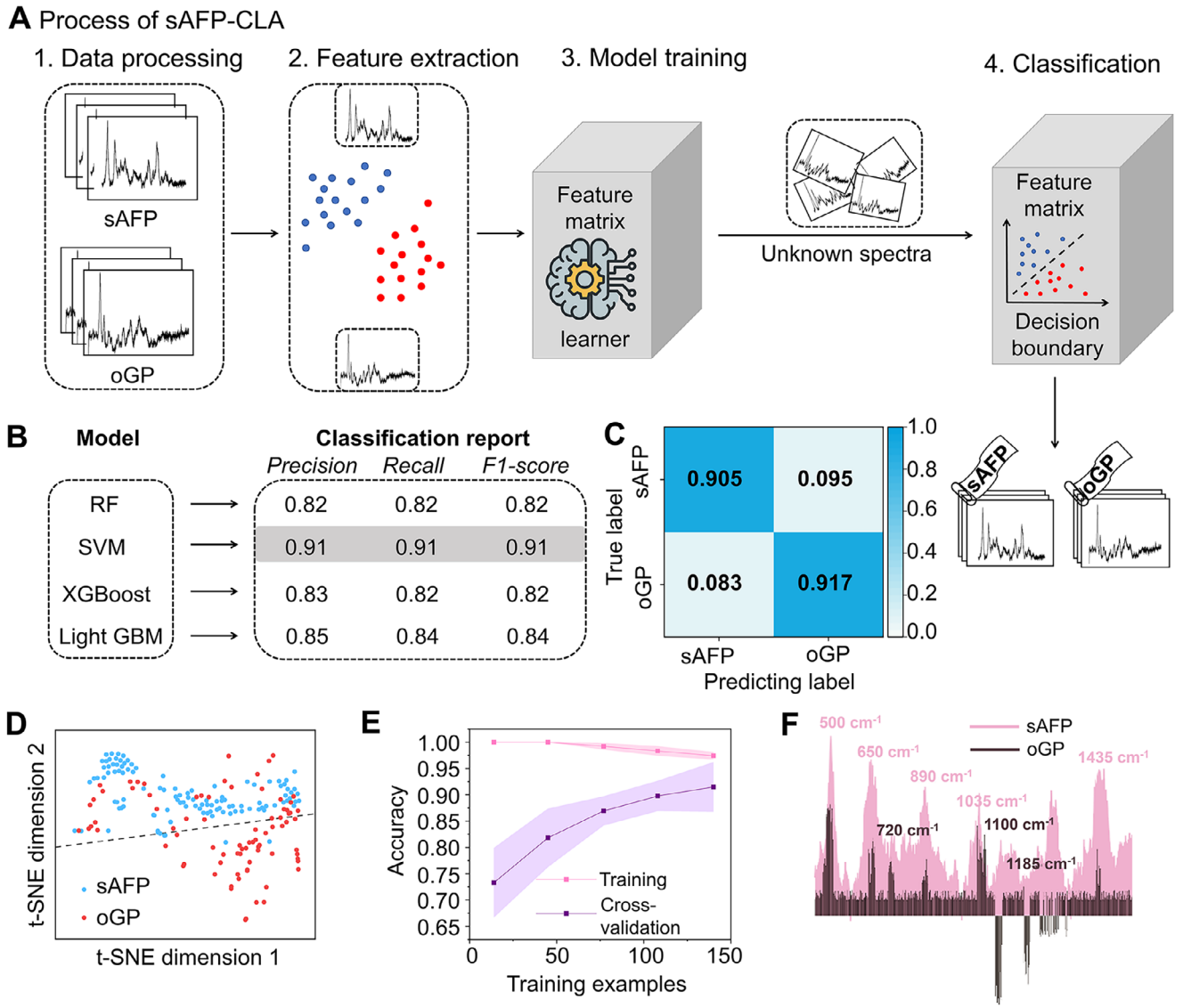

FIGURE 1 | Classification of sAFP by sAFP-CLA. (A) Schematic illustration of the process of sAFP-CLA. The raw Raman spectral data were first processed by Whittaker smoothing (1) and subsequently processed for feature extraction (2) and model training (3). The unknown spectra collected from different samples were subjected to the trained sAFP-CLA for classification (4). (B) Standard classification reports of SVM, random forest (RF), XGBoost, and LightGBM models. (C) Confusion matrix of the sAFP-CLA-based classification of sAFP. (D) Two-dimensional visualization of the extracted features of sAFP and oGP. (E) Learning curves for training and cross-validation. (F) Feature analysis of the contributions of representative spectral features of sAFP and oGP identified by sAFP-CLA.

the sAFP-CLA model, the Raman peaks at 500 and 1035 cm^{-1} were identified as two of the most discriminative spectral features for distinguishing sAFP-positive from sAFP-negative pixels. The peak-specific channels revealed a marked difference in the areas of positive signals between these two peaks (Figure S17A). With the imaging region fixed, the mean Raman intensity within the positive area was extracted and multiplied by the corresponding positive-signal area to obtain the Raman imaging intensities for quantitative comparison (Figure S17B). As a result, the HepG2 cell exhibited gradually enhanced Raman intensities in both 500 and 1035 cm^{-1} channels along with increased incubation time, while the sorafenib-treated HepG2 cell exhibited weak Raman intensities both in 500 and 1035 cm^{-1} channels. In contrast, the B16 cell exhibited negligible Raman intensities in both 500 and 1035 cm^{-1} channels throughout the incubation period. These results indicated the sAFP detection capability of Au/AgNC-MG, but the imaging results were rough and non-quantitative.

To improve the accuracy of quantification, the sAFP-IPA was established (Figure 2A). Briefly, the raw Raman spectra of single-cell Raman images were subjected to pixel-wise classification by sAFP-CLA to filter out negative pixels (defined as "0") and retain candidate positive regions (defined as "1") (Figure 2A-1). Although sAFP-CLA made decisions based on full-spectrum features, the boundary pixels and local noise may make the most discriminative features at 500 and/or 1035 cm^{-1} indefinite at the single-pixel level. To increase the accuracy, the Raman intensities at 500 and 1035 cm^{-1} were extracted for each pixel within the "1" region and subjected to global Otsu thresholding analysis to generate the sAFP channel

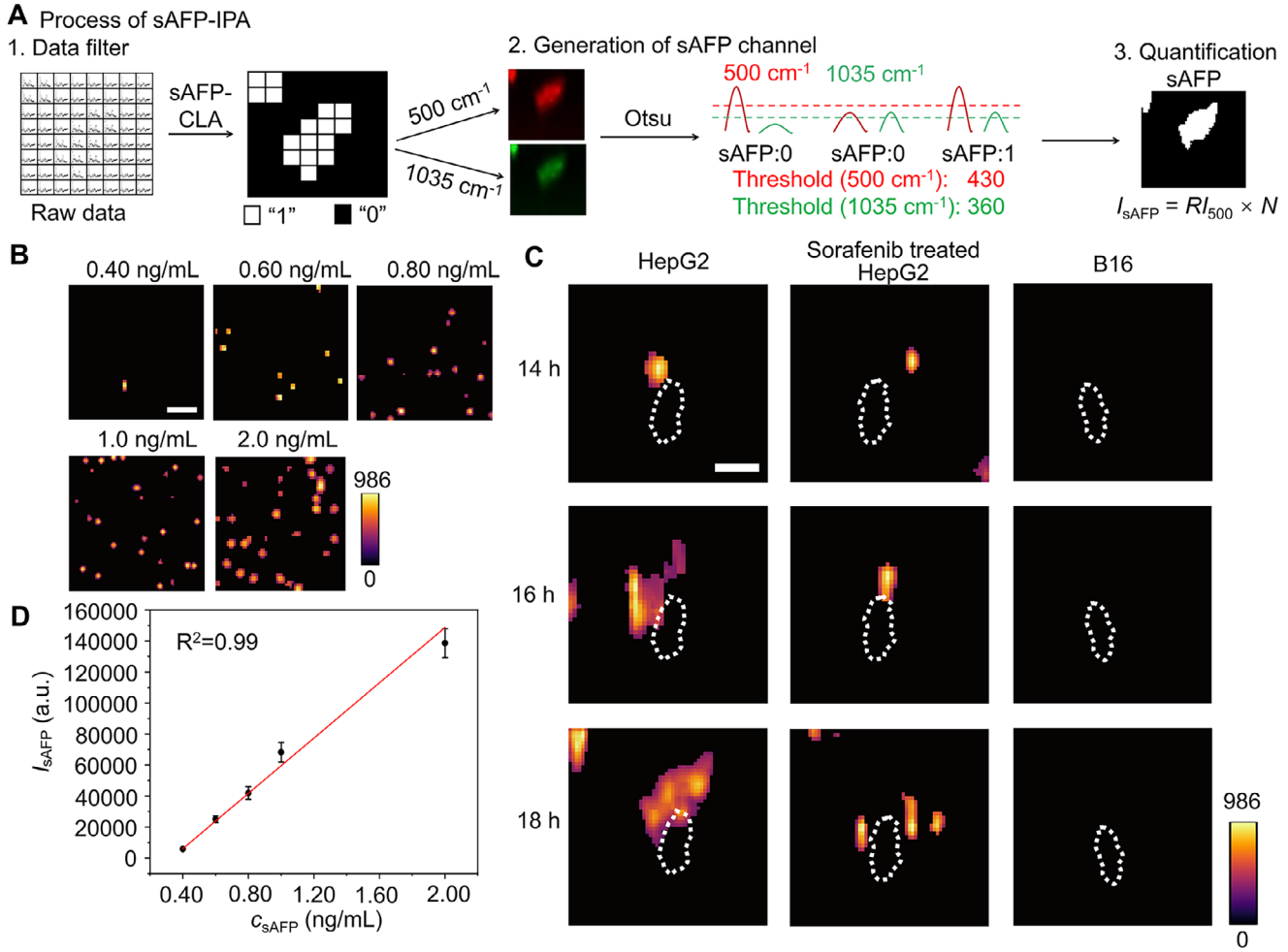

FIGURE 2 | In situ quantification of single-cell secreted sAFP by sAFP-IPA. (A) Schematic illustration of the process of sAFP-IPA. The raw Raman spectra of single-cell Raman images were subjected to pixel-wise classification by sAFP-CLA for data filtering (1), and the Raman intensities at 500 and 1035 cm-1 were extracted and subjected to global Otsu thresholding analysis to generate the sAFP channel (2). The sAFP intensity in the sAFP channel was calculated for quantification of single-cell secreted sAFP (3). (B) sAFP channels of 1.8 × 107 particles/mL of Au/AgNC-MG incubated with different concentrations of standard sAFP at 37°C for 12 h. The white dotted circle indicated the location of a single cell. Scale bars, 20 μm. (C) sAFP channels of singly-seeded HepG2, sorafenib-treated HepG2, and B16 cells after incubation with 1.8 × 107 particles/mL of Au/AgNC-MG at 37°C for 14, 16, and 18 h. Scale bars, 20 μm. (D) Standard curve of I_{sAFP} from (B) *vs* sAFP concentration, mean ± SD, n = 3.

(Figure 2A-2) [43]. To determine intensity thresholds, the Raman images of standard sAFP samples were collected by confocal laser scanning Raman imaging of 1.8 × 10^7 particles/mL of Au/AgNC-MG after incubation with different concentrations of standard sAFP at 37°C for 12 h (Figure S18A). The raw Raman images of standard sAFP samples were also processed with the data filter (Figure 2A-1). According to the scatter plots of the extracted Raman intensities at 500 and 1035 cm^{-1} for different concentrations of standard sAFP (Figure S18B), the vertical and horizontal lines indicate that the global Otsu-derived intensity thresholds were 430 and 360 for Raman intensities at 500 and 1035 cm^{-1}, respectively. The threshold lines also exhibited good separation of the scatter plots of the extracted Raman intensities at 500 and 1035 cm^{-1} of HepG2, sorafenib-treated HepG2, and B16 cells (Figure S19), which indicated the improvement of accuracy of sAFP classification. Thus, only pixels with Raman intensities that simultaneously exceeded the two thresholds were identified as sAFP positive (defined as "sAFP:1"), otherwise, they were identified as sAFP negative (defined as "sAFP:0") (Figure 2A-2).

According to this rule, the sAFP channels in the Raman images of standard sAFP (Figure 2B) and different cells (Figure 2C) were generated. To achieve quantification, the sAFP intensity (I_{sAFP}) in the sAFP channel was calculated by multiplying the average Raman intensity at 500 cm^{-1} (RI_{500}) by the number of pixels (N) within the "sAFP:1" region (Figure 2A-3).

The standard curve of sAFP quantification was generated from the sAFP channels of standard sAFP (Figure 2D), which exhibited a good linear correlation between the I_{sAFP} and sAFP concentration. According to the standard curve (Figure 2D) and the I_{sAFP} of different cells (Figure S20A–C), the single HepG2 cell could secrete 750 ± 57 pg/mL of sAFP after 14 h of incubation, which increased to 1848 ± 166 pg/mL after 18 h. The sorafenib treatment could inhibit the sAFP secretion to 1049 ± 93 pg/mL after 18 h of incubation, while the B16 cells did not secrete any measurable sAFP throughout the incubation period (Figure S20D). Thus, the developed sAFP-IPA could dynamically quantify the amounts of single-cell secreted sAFP from different cells.

2.4 | Clinical HCC Risk Assessment

Although the developed sAFP-CLA and sAFP-IPA could successfully classify and quantify single-cell secreted sAFP, the application of these algorithms to clinical HCC risk assessment requires more interpretable and decision-support information from complex serum samples. The key challenge is that serum AFP level alone lacks specificity for reliable HCC risk assessment, particularly for AFP-negative HCC patients (serum AFP < 20 ng/mL) [44]. Furthermore, elevated AFP levels also occur in other liver malignancies such as intrahepatic cholangiocarcinoma (ICC), raising the demand of differential diagnostic methods. As glycosylation, especially sialylation, is highly associated with various malignancies, a deeper classification of the sAFP Raman fingerprints of the serum samples from different clinical liver malignancies can offer a reliable route to solve these issues. Here, a sAFP-based clinical HCC risk assessment algorithm (sAFP-RAA) was developed and trained on 168 clinical residual serum samples from 41 AFP-positive HCC patients (AFP^+HCC), 39 AFP-negative HCC patients (AFP^-HCC), 23 ICC patients (ICC), and 65 healthy individuals as controls (Con). The use of residual serum samples collected after routine clinical testing and associated clinical data was approved by the Ethics Committee of the First Affiliated Hospital of Nanjing Medical University (approval no. 2019-SR-156), and no additional blood was collected for this study. Written informed consent was obtained from all participants, and the study was conducted in accordance with the Declaration of Helsinki. Each serum sample was directly incubated with 1.8×10^7 particles/mL of Au/AgNC-MG at 37°C for 2 h and subjected to Raman detection (Scheme 1C). In the sAFP-RAA workflow (Figure 3A), the raw Raman spectra were first subjected to independent baseline corrections, which were then denoised and smoothed (Figure 3A-1). Subsequently, peak positions in the fingerprint region were coarsely localized by local-maximum detection. The peak centers were then refined by local Gaussian fitting within a predefined window around each peak, yielding more accurate peak locations and peak heights (Figure 3A-2) [45]. To improve feature reliability, the intensities of peaks output by sAFP-CLA at 650, 720, 890, 1035, 1100, 1185, and 1435 cm^{-1} were normalized to the peak intensity at 500 cm^{-1} to obtain peak-height ratios as features (Figure 3A-3). To balance interpretability, calibration, and clinical applicability, a logistic regression model was selected for the subsequent data processing. After inputting these features and the clinical diagnostic results of the 168 clinical serum samples into the univariable logistic regression models for three binary classification tasks of Con *vs* AFP^+HCC, Con *vs* AFP^-HCC, and Con *vs* ICC, the peak-height ratio features of 650/500, 720/500, and 1035/500 exhibited the acceptable likelihood-ratio test p values ($p < 0.15$) (Figure S21), which were kept in the multivariable selection (Figure 3A-4). In addition, the age of patients and healthy controls was forced as the a priori feature on clinical grounds. The regression coefficients of the retained features were maintained in the final multivariable logistic regression model in RStudio (version 4.5.1) to obtain sAFP-RAA. The assessment nomograms were scaled by proportionally converting the regression coefficients to predictor scores, and the total scores were scaled to the risk percentages (Figure 3B). An online HCC Risk Assessment website was also built to support convenient HCC risk assessment and decision aid (Figure 3A-5).

The performance of sAFP-RAA was first evaluated by receiver operating characteristic (ROC) curves (Figure 3C). Discriminations of Con *vs* AFP^+HCC, Con *vs* AFP^-HCC, and Con *vs* ICC yielded AUC values of 0.86, 0.85, and 0.85, respectively (Figure 3C). Besides, the bias-corrected calibration curves yielded from 1000 bootstrap resamples of Con *vs* AFP^+HCC, Con *vs* AFP^-HCC, and Con *vs* ICC all exhibited close overlap with the apparent and ideal curves, with mean absolute calibration errors of 0.027, 0.011, and 0.035 (Figure S22), which indicated the robust risk assessment capability of sAFP-RAA.

To evaluate the net benefit of sAFP-RAA to guide downstream actions across decision thresholds, the decision curve analysis (DCA) of, the sAFP-RAA-guided strategy (intervention in individuals above the threshold), "treat-all" strategy (intervention in all individuals irrespective of threshold), and "treat-none" strategy (intervention in no individuals) was first performed on the training population (Figure 3D). As a result, the sAFP-RAA-guided strategy consistently achieved a higher net benefit than both the treat-all and treat-none strategies for all the AFP^+HCC, AFP^-HCC, and ICC patients, indicating its fundamental potential as a robust decision-support tool across diverse patient populations.

To further evaluate the clinical application value of the sAFP-RAA-guided strategy, the DCA was performed on clinical data of the general check-up and cirrhosis clinic patient populations of the American Association for the Study of Liver Diseases (AASLD) [44]. As for the general check-up population (Figure 3E), the net benefit of the sAFP-RAA-guided strategy decreased with increasing threshold probability (P_t) and approached the treat-none strategy at task-specific cut-off P_t of 0.14 for AFP^+HCC, 0.10 for AFP^-HCC, and 0.06 for ICC. As for the cirrhosis clinic population (Figure 3F), the net benefit of the sAFP-RAA-guided strategy remained above both treat-all and treat-none strategies for AFP^+HCC and AFP^-HCC across the P_t range up to 0.20, and approached the treat-none strategy at the task-specific cut-off P_t of 0.14 for ICC. These results indicated the decision utility of the sAFP-RAA strategy exhibited a broad decision range for HCC and a relatively limited but efficient decision range for ICC, demonstrating the great clinical application value.

For the convenience of practical clinical application, an online HCC Risk Assessment website was built at https://xyu818.github.io/HCC-Risk-Assessment/ with an easy user interface (Figure S23). The user just needs to treat the patient's serum sample with Au/AgNC-MG at 37°C for 2 h, subject to Raman detection, and then input the age and the raw peak intensities at 500, 650, 720, and 1035 cm^{-1} from the obtained Raman spectrum or the raw Raman spectrum CSV file into corresponding boxes on the web. The user can choose different scenarios, including the general check-up and cirrhosis clinic, and set the decision threshold value. The backend would automatically perform the sAFP-RAA process and display the HCC risk percentages with threshold-based decision recommendations. In addition, the users can also adjust the model coefficients according to the institution-specific baseline prevalence to self-correct diagnostic results. Along with the cumulative clinical data, the sAFP-RAA can be periodically updated and revalidated to improve its robustness and clinical utility.

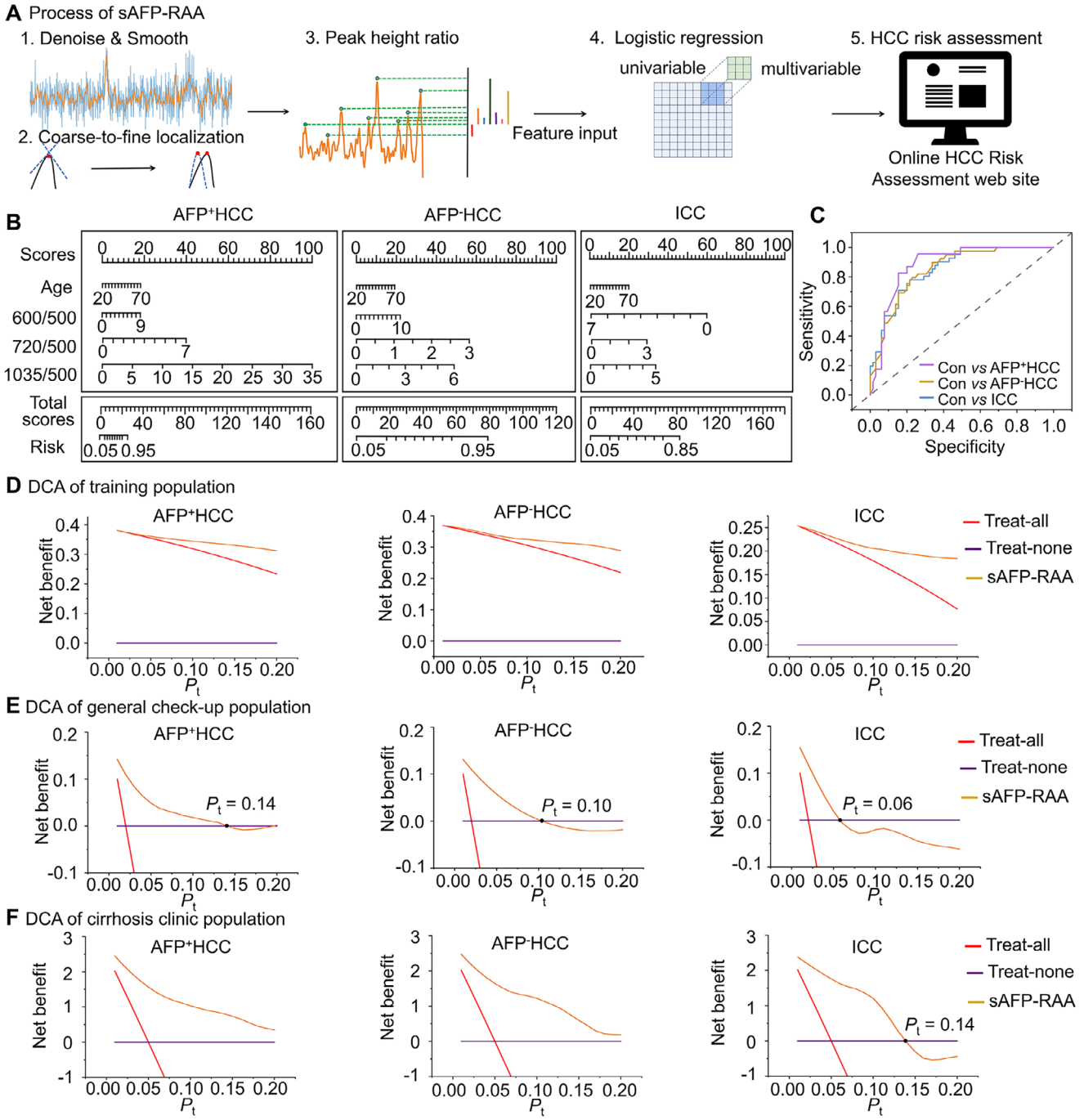

FIGURE 3 | Clinical HCC risk assessment by sAFP-RAA. (A) Schematic illustration of the process of sAFP-RAA. The raw Raman spectra of clinical serum samples were denoised, smoothed (1), and coarsely localized by local-maximum detection (2). The peak-height ratios were calculated and collected as features (3), which were input to logistic regression analysis with age as a priori features (4). The regression coefficients of the retained features were maintained in the final multivariable logistic regression model to obtain sAFP-RAA, which was used to build an online HCC Risk Assessment website (5). (B) Assessment nomograms of AFP+HCC, AFP-HCC, ICC. (C) ROC curves of the discrimination of Con vs AFP+HCC, Con vs AFP-HCC, and Con vs ICC. (D-F) DCA of the treat-all, treat-none, and sAFP-RAA guided strategy performed on the training population (D), the AASLD general check-up population (E), and the AASLD cirrhosis clinic patient population (F).

3 | Conclusion

In conclusion, this work proposes a general paradigm composed of an elaborately constructed Au/AgNC-MG and a series of established ML algorithms. The Au/AgNC-MG exhibits highly specific capture and sensitive quantification of sAFP due to dual aptamer-based recognition and the heterogeneous bimetallic SERS system. The ML algorithms comprehensively assist the quantification, imaging of single-cell secretion, and clinical risk assessment of HCC from the sAFP aspects. The built online HCC Risk Assessment website exhibits convenient clinical practical application and potential updating and revalidation capability with cumulative clinical data. By simply replacing the corresponding recognition components, the proposed general paradigm can

theoretically be extended for any other disease markers, providing a powerful and comprehensive platform for disease mechanism research and clinical applications.

Acknowledgements

This work was financially supported by the National Natural Science Foundation of China (22474057), State Key Laboratory of Analytical Chemistry for Life Science (5431ZZXM2604).

Conflicts of Interest

The authors declare no conflicts of interest.

Data Availability Statement

The data that support the findings of this study are openly available in GitHub at https://github.com/Xyu818/sAFP-Raman-Algorithm.

References

1. J. M. Llovet, R. K. Kelley, A. Villanueva, et al., "Hepatocellular Carcinoma," *Nature Reviews Disease Primers* 7 (2021): 7.

2. N. Tsuchiya, Y. Sawada, I. Endo, K. Saito, Y. Uemura, and T. Nakatsura, "Biomarkers for the Early Diagnosis of Hepatocellular Carcinoma," *World Journal of Gastroenterology* 21 (2015): 10573–10583, https://doi.org/10.3748/wjg.v21.i37.10573.

3. K. Liu, C. Wu, M. Zhu, et al., "Structural Characteristics of Alpha-fetoprotein, Including N-glycosylation, Metal Ion and Fatty Acid Binding Sites," *Communications Biology* 7 (2024): 505, https://doi.org/10.1038/s42003-024-06219-0.

4. Y. Aoyagi, Y. Suzuki, M. Isemura, et al., "The Fucosylation Index of Alpha-fetoprotein and Its Usefulness in the Early Diagnosis of Hepatocellular Carcinoma," *Cancer* 61 (1988): 769–774, https://doi.org/10.1002/1097-0142(19880215)61:4%3c769::AID-CNCR2820610422%3e3.0.CO;2-M.

5. P. J. Johnson, T. C. W. Poon, N. M. Hjelm, C. S. Ho, C. Blake, and S. K. W. Ho, "Structures of Disease-Specific Serum Alpha-Fetoprotein Isoforms," *British Journal of Cancer* 83 (2000): 1330–1337, https://doi.org/10.1054/bjoc.2000.1441.

6. T. X. Wei, W. W. Zhang, Q. Tan, X. W. Cui, and Z. H. Dai, "Electrochemical Assay of the Alpha Fetoprotein-L3 Isoform Ratio to Improve the Diagnostic Accuracy of Hepatocellular Carcinoma," *Analytical Chemistry* 90 (2018): 13051–13058, https://doi.org/10.1021/acs.analchem.8b04045.

7. P. Chen, P. Jiang, Q. Lin, et al., "Simultaneous Homogeneous Fluorescence Detection of AFP and GPC3 in Hepatocellular Carcinoma Clinical Samples Assisted by Enzyme-free Catalytic Hairpin Assembly," *ACS Applied Materials & Interfaces* 14 (2022): 28697–28705, https://doi.org/10.1021/acsami.2c09135.

8. Z. Li, H. M. Li, D. Y. Deng, R. Liu, and Y. Lv, "Mass Spectrometric Assay of Alpha-Fetoprotein Isoforms for Accurate Serological Evaluation," *Analytical Chemistry* 92 (2020): 4807–4813, https://doi.org/10.1021/acs.analchem.9b03995.

9. A. Cabanettes, L. Perkams, C. Spies, C. Unverzagt, and A. Varrot, "Recognition of Complex Core-Fucosylated N-Glycans by a Mini Lectin," *Angewandte Chemie International Edition* 57 (2018): 10178–10181, https://doi.org/10.1002/anie.201805165.

10. I. Sanz-Martinez, S. Pereira, P. Merino, F. Corzana, and R. Hurtado-Guerrero, "Molecular Recognition of GalNAc in Mucin-Type O-Glycosylation," *Accounts of Chemical Research* 56 (2023): 548–560, https://doi.org/10.1021/acs.accounts.2c00723.

11. P. Li, J. Pang, S. Xu, H. He, Y. Ma, and Z. Liu, "A Glycoform-resolved Dual-Modal Ratiometric Immunoassay Improves the Diagnostic Precision for Hepatocellular Carcinoma," *Angewandte Chemie International Edition* 61 (2022): 202113528.

12. Y. Ma, W. J. Guo , Q. Mou, et al., "Spatial Imaging of glycoRNA in Single Cells With ARPLA," *Nature Biotechnology* 42 (2024): 608–616, https://doi.org/10.1038/s41587-023-01801-z.

13. L. Dong, Q. Tan, W. Ye, et al., "Screening and Identifying a Novel ssDNA Aptamer Against Alpha-Fetoprotein Using CE-SELEX," *Scientific Reports* 5 (2015): 15552, https://doi.org/10.1038/srep15552.

14. J. Langer, "Present and Future of Surface-Enhanced Raman Scattering," *ACS Nano* 14 (2020): 28–117, https://doi.org/10.1021/acsnano.9b04224.

15. L. Xu, Z. Lin, H. Tao, et al., "A Dual-Signal Biosensor Based on Surface-Enhanced Raman Spectroscopy for High-Sensitivity Quantitative Detection and Imaging of circRNA in Living Cells," *Biosensors and Bioelectronics* 268 (2025): 116875, https://doi.org/10.1016/j.bios.2024.116875.

16. S. Sinha, S. Jones, A. Pramanik, and P. Ray, "Nanoarchitecture Based SERS for Biomolecular Fingerprinting and Label-Free Disease Markers Diagnosis," *Accounts of Chemical Research* 49 (2016): 2725–2735, https://doi.org/10.1021/acs.accounts.6b00384.

17. H. He, M. Cao, X. Yue, M. Xu, L. Wang, and B. Ren, "Collaborative Low-Rank Matrix Approximation-Assisted Fast Hyperspectral Raman Imaging and Tip-Enhanced Raman Spectroscopic Imaging," *Analytical Chemistry* 93 (2021): 14609–14617, https://doi.org/10.1021/acs.analchem.1c02071.

18. H. KHW, H. Lai, R. Zhang, et al., "SERS-Based Droplet Microfluidic Platform for Sensitive and High-Throughput Detection of Cancer Exosomes," *ACS Sensors* 9, no. 9 (2024): 4860–4869.

19. S. Laing, S. Dennison, K. Faulds, and D. Graham, "Surface Enhanced Raman Scattering for Biomolecular Sensing in Human Healthcare Monitoring," *ACS Nano* 19 (2025): 8381–8400, https://doi.org/10.1021/acsnano.4c15877.

20. J. Kim, J. Kim, K. Choi, J. Park, and J. Nam, "Open Cross-gap Gold Nanocubes With Strong, Large-Area, Symmetric Electromagnetic Field Enhancement for on-Particle Molecular-fingerprint Raman Bioassays," *Journal of the American Chemical Society* 146 (2024): 14012–14021, https://doi.org/10.1021/jacs.4c02099.

21. Y. Wang, C. Ma, X. Zhao, et al., "Self-Assembled Hydrophobic Confinement Coupled With Calcium Coordination Enables Selective and Label-Free SERS Detection of Urinary Biomarkers in Complex Samples," *Advanced Functional Materials* 36 (2025): 14570.

22. Y. Hang, A. Wang, and N. Wu, "Plasmonic Silver and Gold Nanoparticles: Shape- and Structure-Modulated Plasmonic Functionality for Point-of-Caring Sensing, Bio-Imaging and Medical Therapy," *Chemical Society Reviews* 53 (2024): 2932–2971, https://doi.org/10.1039/D3CS00793F.

23. S. Schlcker, "Surface-Enhanced Raman Spectroscopy: Concepts and Chemical Applications," *Angewandte Chemie International Edition* 53 (2014): 4756–4795, https://doi.org/10.1002/anie.201205748.

24. T. Itoh, M. Prochazka, Z. Dong, et al., "Toward a New Era of SERS and TERS at the Nanometer Scale: From Fundamentals to Innovative Applications," *Chemical Reviews* 123 (2023): 1552–1634, https://doi.org/10.1021/acs.chemrev.2c00316.

25. A. Li, X. Mo, Y. Lu, et al., "Digital SERS Immunoassay of Interleukin-6 Based on Au@Ag-Au Nanotags," *Biosensors and Bioelectronics* 270 (2025): 0956–5663, https://doi.org/10.1016/j.bios.2024.116973.

26. D. Chen, Y. Wang, Y. Wei, et al., "Size-Coded Hydrogel Microbeads for Extraction-Free Serum Multi-miRNAs Quantifications With Machine-Learning-Aided Lung Cancer Subtypes Classification," *Nano Letters* 25 (2025): 453–460, https://doi.org/10.1021/acs.nanolett.4c05233.

27. S. Zhou, J. Li, K. Gilroy, et al., "Facile Synthesis of Silver Nanocubes With Sharp Corners and Edges in an Aqueous Solution," *ACS Nano* 10 (2016): 9861–9870, https://doi.org/10.1021/acsnano.6b05776.

28. H. Trinh, S. Kim, S. Yun, L. Huynh, and S. Yoon, "Combinatorial Approach to Find Nanoparticle Assemblies With Maximum Surface-

enhanced Raman Scattering," *ACS Applied Materials & Interfaces* 16 (2024): 1805–1814, https://doi.org/10.1021/acsami.3c14487.

29. K. Jiao, Q. Yan, L. Guo, et al., "Poly-Adenine-Based Spherical Nucleic Acids for Efficient Live-Cell MicroRNA Capture," *Angewandte Chemie International Edition* 60 (2021): 14438–14445, https://doi.org/10.1002/anie.202017039.

30. D. Makharadze, L. Valle, R. Katsarava, and J. Puiggali, "The Art of PEGylation: From Simple Polymer to Sophisticated Drug Delivery System," *International Journal of Molecular Sciences* 26 (2025): 3102, https://doi.org/10.3390/ijms26073102.

31. X. Ma, X. Li, G. Luo, and J. Jiao, "DNA-functionalized Gold Nanoparticles: Modification, Characterization, and Biomedical Applications," *Frontiers in Chemistry* 10 (2022): 1095488, https://doi.org/10.3389/fchem.2022.1095488.

32. R. Flaherty, A. Bergin, E. Flampouri, et al., "Mammalian Cell Culture for Production of Recombinant Proteins: A Review of the Critical Steps in Their Biomanufacturing," *Biotechnology Advances* 43 (2020): 107552, https://doi.org/10.1016/j.biotechadv.2020.107552.

33. C. Dunbar, M. Kushnir, and Y. Yang, "Glycosylation Profiling of the Neoplastic Biomarker Alpha Fetoprotein Through Intact Mass Protein Analysis," *Journal of Proteome Research* 22 (2023): 226–234, https://doi.org/10.1021/acs.jproteome.2c00656.

34. G. Roberts, "Histochemical Detection of Sialic Acid Residues Using Periodate Oxidation," *The Histochemical Journal* 9 (1977): 97–102, https://doi.org/10.1007/BF01007012.

35. X. R. Li, S. J. Martin, Z. Chinoy, et al., "Label-Free Detection of Glycan–Protein Interactions for Array Development by Surface-Enhanced Raman Spectroscopy (SERS)," *Chemistry—A European Journal* 22 (2016): 11180–11185, https://doi.org/10.1002/chem.201602706.

36. Z. Wang, J. Ye, K. Zhang, et al., "Rapid Biomarker Screening of Alzheimer's Disease by Interpretable Machine Learning and Graphene-assisted Raman Spectroscopy," *ACS Nano* 16 (2022): 6426–6436, https://doi.org/10.1021/acsnano.2c00538.

37. N. Maiti, M. Apetri, M. Zagorski, P. Carey, and V. Anderson, "Raman Spectroscopic Characterization of Secondary Structure in Natively Unfolded Proteins: α-Synuclein," *Journal of the American Chemical Society* 126 (2004): 2399–2408, https://doi.org/10.1021/ja0356176.

38. N. Shah, O. Lyandres, J. Walsh, M. Glucksberg, and R. Duyne, "Lactate and Sequential Lactate−Glucose Sensing Using Surface-Enhanced Raman Spectroscopy," *Analytical Chemistry* 79 (2007): 6927–6932, https://doi.org/10.1021/ac0704107.

39. I. Pence and A. Jansen, "Clinical Instrumentation and Applications of Raman Spectroscopy," *Chemical Society Reviews* 45 (2016): 1958–1979, https://doi.org/10.1039/C5CS00581G.

40. L. Pont, V. Kuzyk, F. Benavente, et al., "Site-Specific N -Linked Glycosylation Analysis of Human Carcinoembryonic Antigen by Sheathless Capillary Electrophoresis–Tandem Mass Spectrometry," *Journal of Proteome Research* 20 (2021): 1666–1675, https://doi.org/10.1021/acs.jproteome.0c00875.

41. P. Eilers, "A Perfect Smoother," *Analytical Chemistry* 75 (2003): 3631–3636, https://doi.org/10.1021/ac034173t.

42. Y. Jia, Y. Xing, and M. Yang, "Efficacy of Sorafenib Combined With Interventional Therapy on Primary Liver Cancer Patients and Its Effect on Serum AFP, VEGF, and GGT," *Journal of Oncology* 2021 (2021): 9120265, https://doi.org/10.1155/2021/9120265.

43. N. Otsu, "A Threshold Selection Method From Gray-Level Histograms," *IEEE Transactions on Systems, Man, and Cybernetics* 9 (1979): 62–66, https://doi.org/10.1109/TSMC.1979.4310076.

44. A. Singal, J. Llovet, M. Yarchoan, et al., "AASLD Practice Guidance on Prevention, Diagnosis, and Treatment of Hepatocellular Carcinoma," *Hepatology* 78 (2023): 1922–1965, https://doi.org/10.1097/HEP.0000000000000466.

45. J. Lu, M. Trnka, S. Roh, et al., "Improved Peak Detection and Deconvolution of Native Electrospray Mass Spectra From Large Protein Complexes," *Journal of the American Society for Mass Spectrometry* 26 (2015): 2141–2151, https://doi.org/10.1007/s13361-015-1235-6.

Supporting Information

Additional supporting information can be found online in the Supporting Information section.

Supporting File: smtd70822-sup-0001-SuppMat.pdf.